Improved photocatalytic Bi_2WO_6/BiOCl heterojunctions: one-step synthesis via an ionic-liquid assisted ultrasonic method and first-principles calculations

Shiwen Zhu,[a, #] Chengyu Yang, [a, #] Feng Li, [a] Taohai Li, [a, *] Meng Zhang [b, *] and Wei Cao[c]

[a]*College of Chemistry, Key Lab of Environment Friendly Chemistry and Application in Ministry of Education, Xiangtan University, Xiangtan, 411105, China*

[b]*Department of Physics, East China University of Science and Technology, Shanghai 200237, China.*

[c]*Nano and Molecular Materials Research Unit, Faculty of Science,University of Oulu, P.O. Box 3000, FIN-90014, Finland*

[*]Correspondence Author. Tel.: +86-731-58292202; fax: +86-731-8292251; *E-mail address*: hnlth@xtu.edu.cn(T. Li); mzhang@ecust.edu.cn(M. Zhang).

#Shiwen Zhu and Chengyu Yang contributed equally to this research and should be considered co-first authors.

Abstract:

Bi_2WO_6/BiOCl heterojunctions with high photocatalytic activity and photocurrent property were synthesized via an ionic-liquid assisted ultrasonic irradiation at room temperature. The ionic liquid 1-butyl-3-methylimidazolium chloride ([BMIM]Cl) was used as the Cl source. Modifications of heterojunction structures and properties were realized just by changing the amount of [BMIM]Cl. Photocatalytic activities of Bi_2WO_6/BiOCl heterojunctions enable fast degradations of 2,4-dinitrophenol solution (DNP), rhodamine B (RhB) and quinoline blue (QB) under visible light and sunlight irradiation. Through first-principles calculations, the Bi-O bonding was found as junction structures at the interface, leading to band intercalations between the two parts besides the interface. Efficient charge (hole) transfers to two sides of the tungstate and chloride were enabled through interface during photocatalytic processes, resulting in longer electron-hole separations, and enhanced catalytic activities under sunlight radiation. The mechanism is crosschecked with transient photocurrent results where the BiOCl-Bi_2WO_6 heterojunction possess higher photocurrent than pure Bi_2WO_6 or BiOCl, ascribed to inhibition of electron-hole recombination in the photo processes.

Keywords: Bi_2WO_6/BiOCl; heterojunctions; Ionic-liquid; Ultrasonic; Photocatalytic

1. Introduction

Semiconductor photocatalyst has been widely used for environmental pollutants removal and solar energy conversion [1-3]. Recently, Bi_2WO_6 has attracted extensive attention due to its narrow band gap (the band gap is 2.8eV) and photocatalytic activity under visible light [4-6]. However, the photocatalytic activity of Bi_2WO_6 is low because of its high recombination probability between photogenerated electrons and holes, which limits its application in the fields of environmental protection. Fortunately, many attempts have been made to overcome these disadvantages, including controlling the morphologies [7,8], forming heterojunctions [9-11], and coupling with oxygen-evolution catalysts [12]. To be noted, the heterojunctions composed of two or more photocatalysts may efficiently promote the interfacial charge transfer and reduce the recombination of photoinduced electron-hole pairs, so it can improve energy transfer efficiency and enhance photocatalytic activity. So far, a lot of heterojunctions have been synthesized, such as WO_3/Bi_2WO_6 [13], TiO_2/Bi_2WO_6 [14,15], Bi_2O_3/Bi_2WO_6 [16], $BiOBr/Bi_2WO_6$ [17] and Bi_2S_3/Bi_2WO_6 [10].

Another bismuth compound, the BiOCl, has also unique materials properties such as high stability and relatively superior photocatalytic ability [18-20]. The crystal lattice of BiOCl matches well with that of Bi_2WO_6 [21], which makes it easy form Bi_2WO_6/BiOCl heterojunction. Up to now, only the solvothermal method has been used to synthesize Bi_2WO_6/BiOCl heterojunction. However, the reaction conditions are very rigorous, and high pressure, high reaction temperature and long reaction time are always needed. Therefore, development a mild and environment-friendly method for the synthesis of Bi_2WO_6/BiOCl is of great importance for broadening and improving their industrial applications.

In recent years, ultrasonic synthesis method has attracted considerable attentions owing to its rapid reaction rate, high efficiency, mild reaction conditions, high purity of products and environmentally friendly properties. The primary mechanism for sonochemistry is acoustic cavitation, including

formation, growth, and implosive collapse of bubbles in a liquid. The rapid collapse of such bubbles results in intense local heating, high pressure, and extremely rapid cooling rates [22]. The unusual properties can drive many chemical reactions, such as redox, dissolution, and promotion of polymerization. The solvent of sonochemical reactions is critical, because the physical and chemical effects of cavitation are highly dependent on the contents of the collapsing bubble. Undoubtedly, solvents with low vapour pressure can be a good choice, which can minimize the participation of the solvent in reaction and maximize the temperatures and pressures of bubbles collapse [23]. Ionic liquids (ILs) have been widely used for the synthesis of semiconductor inorganic materials due to its high thermal stability, excellent dissolving ability, and negligible vapour pressure [24-31], which are potential solvents for sonochemical reactions.

Herein, combining the advantages of both ILs and ultrasound, ionic-liquid assisted ultrasonic method was developed to prepare Bi_2WO_6/BiOCl heterojunctions at room temperature. Ionic liquid 1-butyl-3-methylimidazolium chloride ([BMIM]Cl) mainly used as a Cl source. And the photocatalytic activities were evaluated by the degradation of rhodamine B (RhB) and quinoline blue (QB) under visible light irradiation and sunlight irradiation. The obtained Bi_2WO_6/BiOCl heterojunctions exhibited high photocatalytic activity and stability. A first-principles calculation was carried out to explicate interfacial structures and band structures leading to materials properties. A possible photocatalytic mechanism for the enhanced photocatalytic activity of Bi_2WO_6/BiOCl was proposed. Transient photocurrent measurements were also carried out to further explicate charge transfer responses of the heterojunctions under visible light radiation.

2. Experimental Section

2.1. Synthesis of Bi_2WO_6/BiOCl heterojunctions

All of the chemical reagents were analytical purity and used without further purification. The ionic liquid 1-butyl-3-methylimidazolium chloride ([BMIM]Cl) was added to the water solution (20 mL) of $Bi(NO_3)_3 \cdot 5H_2O$ (4.851

g, 10 mmol) and $Na_2WO_4 \cdot 2H_2O$ (2.42 g, 7 mmol). (The details were shown in Table 1). And the mixture was kept stirring for 20 min at room temperature. Afterwards, the mixture was transferred to ultrasonic bath (100 W, 40 kHz, Shu Mei KQ-250DB, china) and treated for 2 h. The precipitate was obtained after ultrasonic irradiation for 2 h, and it was purified by filtration and washing with water and ethanol several times. Finally, the products were dried at 70 ^oC for 12 h. Depending on the dosage of [BMIM]Cl (0 g, 0.5 g, 1 g), different composites can be synthesized and labelled as S1, S2 and S3, respectively.

For the purpose of comparison, sample S4 was prepared under the same conditions with sample S2 expect for ultrasonic treatment. To investigate the role of ionic liquid [BMIM]Cl in the synthesis of Bi_2WO_6/BiOCl composites, KCl was used as the Cl source for the preparation of Sample S5. (The detailed conditions are available in Table 1.

Table 1

samples	$Bi(NO_3)_3 \cdot 5H_2O$ /g	$Na_2WO_6 \cdot 2H_2O$ /g	[BMIM]Cl /g	KCl /g	reaction condition
S1	4.85	2.42	0	0	ultrasound
S2	4.85	2.42	0.5	0	ultrasound
S3	4.85	2.42	1.0	0	ultrasound
S4	4.85	2.42	0.5	0	without ultrasound
S5	4.85	2.42	0	0.21	ultrasound

2.2. Characterization

The crystal structure of the prepared samples was characterized by powder X-ray diffraction (XRD) on a D8 ADVNCE apparatus diffractometer at 40 kV and 40 mA with Cu-Kα radiation. FT-IR spectrum was recorded in the range of 600-4000 cm^{-1} on a Shimadzu-8400S spectrometer. The composition of the as-prepared product was analyzed by an energy-dispersive X-ray spectroscopy (EDS). X-ray photoelectron spectroscopy (XPS) with Al Kα X-rays (hv = 1486.6 eV) radiation operated at 150 W (XPS: Thermo ESCALAB 250, USA) was used to investigate the surface properties. The morphologies and microstructures characterizations were performed on the scanning electron

microscopy (SEM, JEOL JSM-6700F) and transmission electron microscopy (TEM, JEOL JEM-2100F). Nitrogen adsorption–desorption isotherms were obtained on a nitrogen adsorption apparatus (TRISTAR II3020, USA). UV-vis diffuse reflectance spectra were obtained for the dry pressed disk samples with a UV-visible spectrophotometer (UV-2550, Shimadzu, Japan) using $BaSO_4$ as a reference.

2.3. Photocatalytic activity measurement

Photocatalytic activities of the products (50 mg) were evaluated by the degradation of the colorless dye 2,4-dinitrophenol solution (DNP, 10 mg/L, 50 mL), RhB solution (5 mg/L, 50 mL) and quinoline blue solution (5 mg/L, 50 mL) under visible light (Xe-lamp, 300 W with the 400 nm cutoff filter) and sunlight (Xiangtan, China, 14:30-16:30, 2014/07/10) irradiation for a period time. To eliminate the adsorption/desorption equilibrium effects of RhB and QB, all of the samples were magnetically stirred in dark for 30 min before the irradiation. The solution (4 mL) was taken out periodically and centrifuged to remove the catalysts. The UV-visible absorption spectra were recorded on a Lambda 25 UV-vis spectrophotometer (Perkin-Elmer, USA). The maximum absorption peak of DNP was at 360 nm, RhB was at 553 nm and QB was at 638 nm, which was used to detect the degradation of RhB and QB. The spectra scan range was 300-800 nm.

2.4. Determination of reactive species

To investigate the possible reactive species involved in the photocatalytic process, the trapping experiments of active species were conducted. Various scavengers, including benzoquinone (BQ, 2 mmol/L), tertiary butanol (t-BuOH, 10 mmol/L) and potassium iodide (KI, 5 mmol/L) were introduced into the solution of QB (5 mmg/L) to trap the active species. The experimental procedures were as follows: the photocatalyst (0.05 g) was dispersed in 50 mL of the QB (5 mg/L) aqueous solution. The solution was irradiated under visible light and 4 mL of sample

was extracted periodically, centrifuged and measured on Lambda 25 UV-vis spectrophotometer.

2.5. Computational Methods

All theoretical calculations were performed through the density functional theory (DFT) by using the Cambridge Serial Total Energy Package (CASTEP) package [32]. The exchange–correlation functional is treated within the generalized gradient approximation (GGA), in the form of Perdew–Burke–Ernzerhof (PBE) functional [33]. The convergence tolerance of the energy was set to 10^{-6} eV and the energy cutoff of the plane wave basis set was set to 600 eV. The Brillouin zone is represented by sets of 3×3×1 k-points to study electronic properties. For comparison purposes, the band structures were calculated along the special lines connecting the following high-symmetry points: G (0,0,0), Q (0,0.5,0.5), Z (0,0,0.5), M (0.5,0.5,0), F (0,0.5,0), and A (0.5,0.5,0.5) in the k-space.

The unit cells for pristine Bi_2WO_6 and BiOCl were firstly relaxed and the optimized lattice constants are a=5.436Å, b=5.457Å, c=16.427Å for the Bi_2WO_6 and a=b=3.878Å, c=15.824Å for the BiOCl, respectively. Out results are in good agreements with experimental and previous theoretical results [21,34,35]. Then the heterostructure of two materials Bi_2WO_6/BiOCl was built based on HRTEM results. The steps are similar to the Shan group [21,36]. It contains 84 atoms including 6 W atoms, 8 Cl atoms, 22 Bi atoms, and 48 O atoms. A 10 Å vacuum region was adopted to avoid the interactions between top and bottom atoms in the periodic slab.

2.6. Photoelectrochemical measurements

The photocurrent plots were recorded on an electrochemical analyzer (CHI660D, CHI Shanghai). The instrument was operated in a standard three-electrode configuration. The as-prepared samples (S1, S2, S3) were used as the working electrode. The Pt foil was used as the counter electrode, and saturated Ag/AgCl was used as the reference electrode. A 0.5M Na_2SO_4 aqueous solution was used as the electrolyte. A Xenon lamp was used as the light source for the PEC measurement.

3. Results and discussion

3.1. Structural analysis

First, the effect of ionic liquid on the structures of heterojunctions was investigated. From Fig. 1a, when no ionic liquid was added, it can be seen that all the peaks of the product are readily indexed to the Bi_2WO_6 (S1) (JCPDS NO. 39-0256), and the diffraction peaks at 10.8 and 28.3 are attributed to the {020} and {131} crystal faces. The result suggests the product has an amorphous structure. The coexistence of Bi_2WO_6 and BiOCl was observed in Fig. 1b with the addition of 0.5 g [BMIM]Cl during the preparation. The XRD pattern in Fig. 1b suggests that Bi_2WO_6/BiOCl heterojunction (S2) was well crystallized, and no characteristic peaks of other impurities were observed, demonstrating that the Bi_2WO_6/BiOCl sample is only composed of orthorhombic Bi_2WO_6 and tetragonal BiOCl. When increasing the amount of [BMIM]Cl to 1 g, the structure of the tetragonal phase of BiOCl (S3) (JCPDS No. 06-0249) still existed, while the XRD peaks of Bi_2WO_6 were disappeared, as shown in Fig. 1c. These results suggest that the amount of ionic liquid has a significant effect on the structures of the obtained samples and the structure can be conveniently controlled via the change of amount of ionic liquid during their preparation.

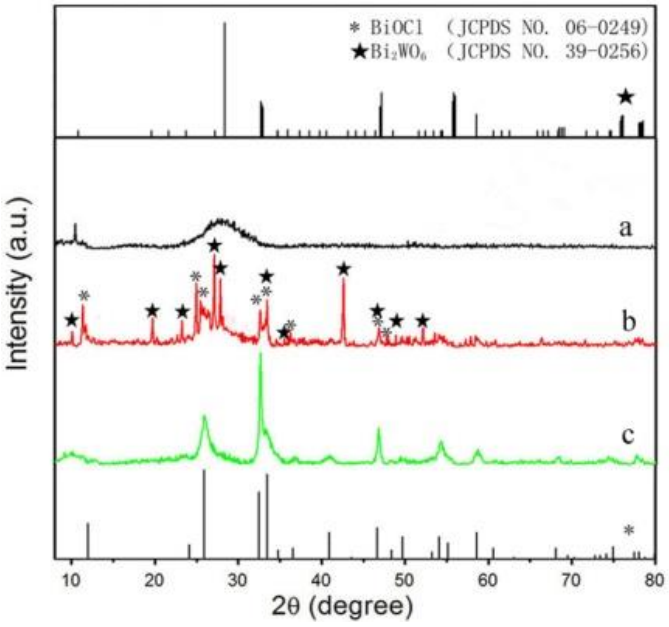

Fig. 1.

Comparing with the sample S2, the sample S4 was obtained in the absence of ultrasound. Fig. 2a shows the XRD pattern of sample S4, where it can be found that only amorphous Bi_2WO_6/BiOCl was formed in the absence of ultrasound. Comparing with sample S2, ILs was replaced by equimolar KCl during the synthetic process of sample S5. Fig. 2b shows the XRD pattern of sample S5, where it can be seen that only the amorphous BiOCl was gained. Therefore, it can be speculated that ionic-liquid assisted ultrasound is helpful for the synthesis of Bi_2WO_6/BiOCl. The primary mechanism for sonochemistry is acoustic cavitation, including formation, growth, and implosive collapse of bubbles in a liquid. The rapid collapse of such bubbles results in intense local heating, high pressure, and extremely rapid cooling rates. The unusual properties can drive chemical reactions. The solvent of sonochemical reactions is critical, because the physical and chemical effects of cavitation are highly dependent on the contents of the collapsing bubble. Therefore, a possible reason is that the negligible vapor pressure of [BMIM]Cl is helpful to bubbles collapse during acoustic cavitation process of the ultrasound, driving high-energy for the chemical reaction. On the other hand, the lower boundary tension of [BMIM]Cl contributes to the high rate of nucleation of products. Moreover, the high ionic conductivity of [BMIM]Cl accelerates the transfer of electron, which simplifies the reaction conditions.

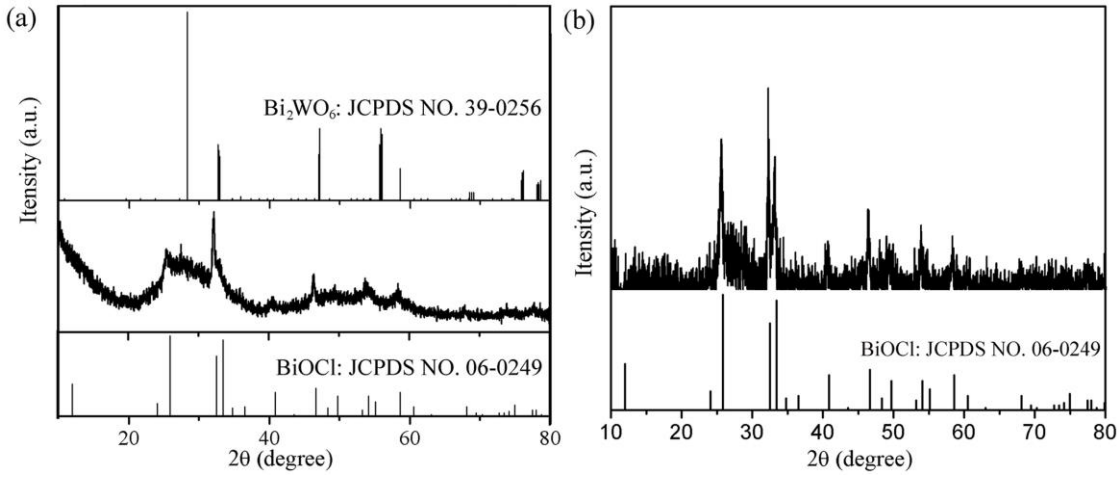

Fig. 2

3.2. FT-IR spectroscopy analysis

Fig. 3 shows the FT-IR spectra of sample S2 and pure [BMIM]Cl. Two peaks of sample S2 at about 3332.7 cm^{-1} and 1614.9 cm^{-1} can be attributed to the stretching and deformation vibration of the O-H groups of chemisorbed and/or physisorbed water molecules. The surface hydroxyl groups from the adsorbed water molecules could enhance the photocatalytic activity. They present the absorption bands of sample S2 at near 1100 cm^{-1}, which are assigned to the Bi-O stretching. In the spectrum of the sample S2, the peaks at 1043 cm^{-1} and 897.5 cm^{-1} are attributed to W-O stretching. The absorption band of sample S2 at 673 cm^{-1} is assigned as the W-O-W stretching. Comparing with the spectrum of [BMIM]Cl, no characteristic peaks of [BMIM]Cl can be found in the spectrum of the sample S2. Therefore, the product of sample S2 didn't contain [BMIM]Cl.

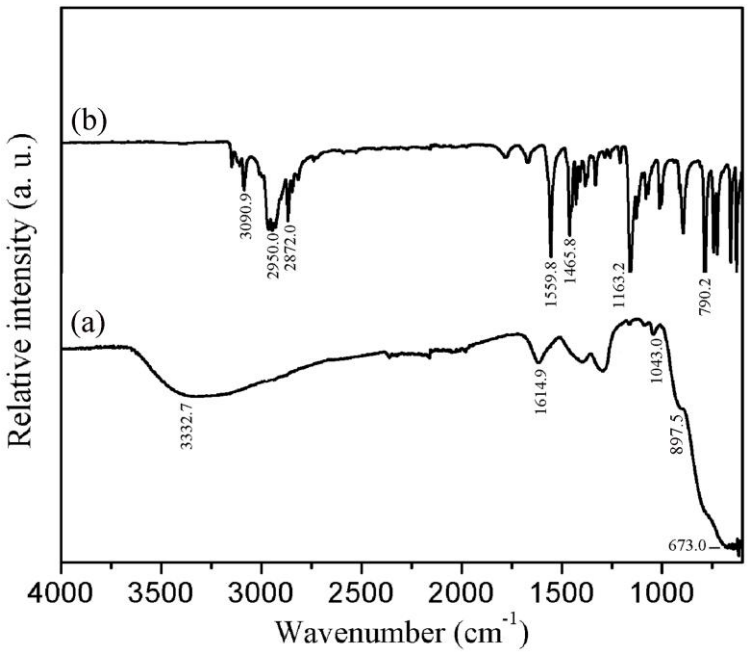

Fig. 3

3.3. Morphological structure

The morphologies of the as-prepared heterojunctions were characterized by SEM. Fig. 4a displays that the Bi_2WO_6 (S1) has an amorphous structure. As shown in Fig. 4b, the as-prepared BiOCl (S3) has typically aggregated into numerous large-size nanoparticles with irregular microsphere morphology. Fig. 4c is the SEM image of the as-prepared Bi_2WO_6/BiOCl heterojunction (S2),

which exhibits a series of diamond microrods with lengths of 5-10 μm and diameters around 1 μm. As shown in the high magnification SEM image of S2 (Fig. 4d), the surface of the microrods was coated with many nanoparticles.

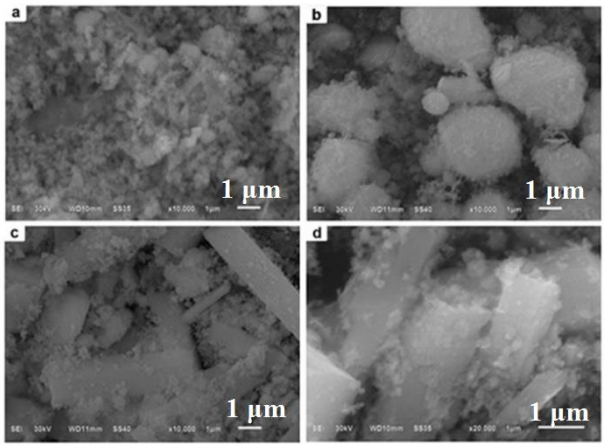

Fig. 4

The morphological structure of the as-prepared Bi_2WO_6/BiOCl heterojunction (S2) was further characterized by TEM and HRTEM (Fig. 5). As shown in Fig. 5, the surface of the microrods is coated by many nanoparticles with diameter of 15-30 nm, which is consistent with the result of SEM. As shown in the HRTEM image of Bi_2WO_6/BiOCl (S2), the values of lattice spacing are measured to be 0.375 nm and 0.315 nm corresponding to the (111) and (131) crystal plane of Bi_2WO_6, respectively. The lattice interlinear spacing of 0.258 nm and 0.220 nm are attributed to the (111) and (112) crystal planes of BiOCl, respectively. These results indicate that the heterojunction interface between BiOCl and Bi_2WO_6 can be formed.

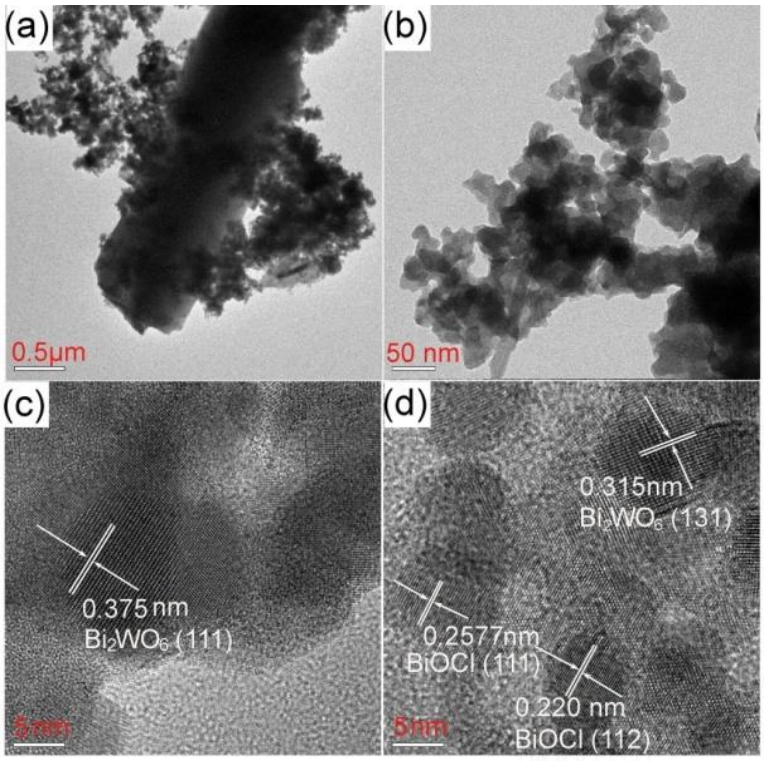

Fig. 5

3.4. XPS and EDS analysis

The elemental composition and electronic states of Bi_2WO_6/BiOCl (S2) powder were investigated by XPS analysis. Fig. 6a is a typical XPS survey spectrum of Bi_2WO_6/BiOCl (S2), where the peaks of Bi4f, W4f, Cl2p, and O1s can be clearly observed. The binding energy at 284.8 eV was attributed to the carbon on the surface of the sample. In the spectrum of W4f, the peaks at 37.15 and 34.9 eV were assigned to the W4f5/2 and W4f7/2, respectively [37]. The XPS spectrum for O1s at a binding energy of 531.2 eV corresponds to the O^{2-} anions in Bi_2WO_6/BiOCl (S2) (Fig. 6c) [38]. Two peaks at 198.9 and 197.8 eV in the spectrum of Cl2p were assigned to the Cl2p1/2 and Cl2p3/2, respectively, which is the characteristic of Cl^- in BiOCl (Fig. 6d) [39]. The characteristic signals of Bi4f5/2 at 164.5 eV and Bi4f7/2 at 159.2 eV can be observed in Fig. 6e [40]. The chemical composition of the Bi_2WO_6/BiOCl (S2) was further confirmed by EDS analysis. As shown in Fig. 6f, Bi, Cl, O and W peaks were observed in this spectrum. The results of the XPS and EDS prove that the

as-prepared samples are the composite of Bi_2WO_6 and BiOCl, in consistent with the results of XRD.

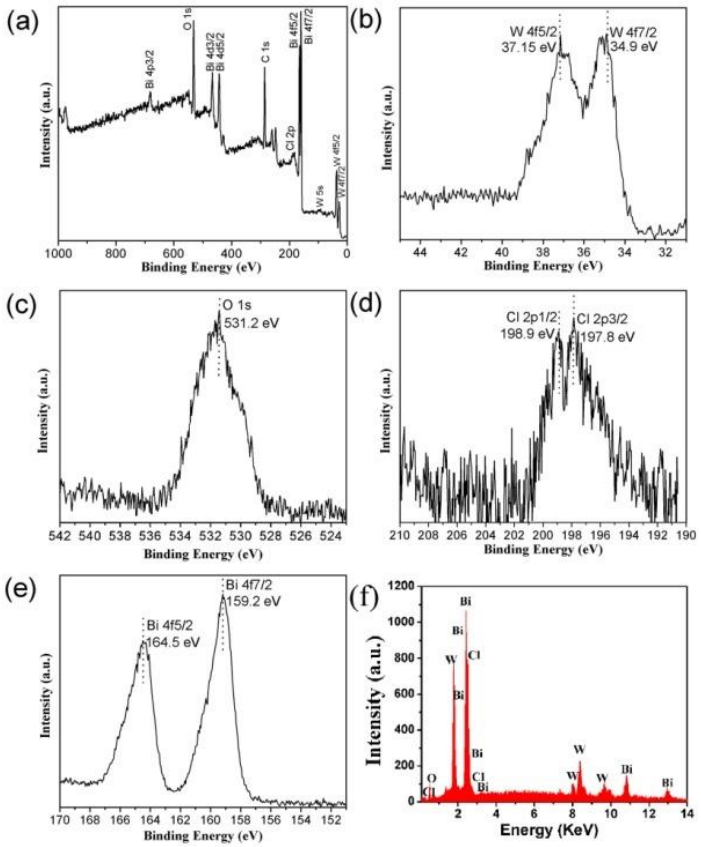

Fig. 6

3.5. Optical properties

Band gap energy is a key factor in determining the photocatalytic activity. The UV–Vis diffuse reflectance spectra of the as-prepared samples and the corresponding band gap energy calculated from a plot of $(ahv)^{1/2}$ versus photon energy (hv) were shown in Fig. 7. All the samples show high absorption from 200 nm to 350 nm with the obvious absorption around 300 nm. The absorption edge was around 400-430 nm, and the band gaps energy of Bi_2WO_6 (S1), Bi_2WO_6/BiOCl (S2), and BiOCl (S3) were calculated to be about 2.88 eV, 2.90 eV and 2.93 eV, respectively. The above results reveal that the absorption edges of Bi_2WO_6 (S1) lie in the visible region, while the absorption edges of Bi_2WO_6/BiOCl (S2) and BiOCl (S3) are near the visible region, which are different with the literutures [41,42], mainly due to their different structures and morphologies.

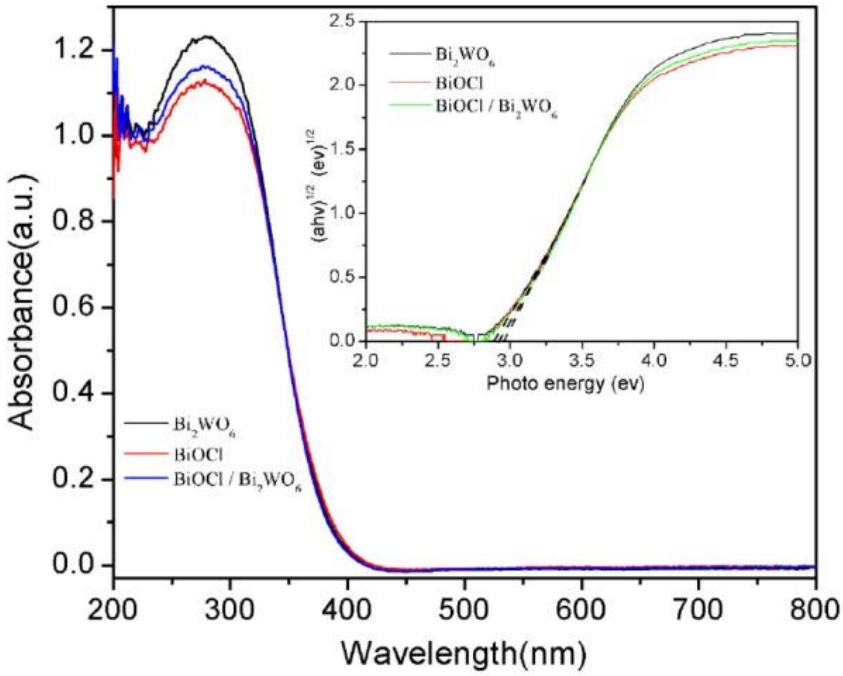

Fig. 7

3.6. BET surface areas and pore size distributions

Besides the band gap energy, the adsorbed reactant on the surface of the semiconductor catalyst is another key factor in determining the photocatalytic activity. Therefore, the specific surface area and the porosity of the as-prepared samples were measured by the nitrogen adsorption-desorption isotherms (Fig. 8). The recorded adsorption and desorption isotherms of all samples display a type IV isotherm. All samples with a distinct hysteresis loop in the range of 0.5-1.0 P/P_0 imply the presence of mesoporous structure (2–50 nm in size) [43,44]. Furthermore, the shapes of hysteresis loops are type H3 (at $p/p_0 > 0.8$), due to the formation of mesopores during the aggregation of particles. The hysteresis loop shifts to about $p/p_0 = 1$, which characteristically indicates the existence of macropores (> 50 nm) [45]. The above results are further confirmed by the pore-size distributions (PSD) of the as-prepared samples (the insets of Fig. 8), where the PSD curve of the BiOCl (S3) and Bi_2WO_6/BiOCl (S2) are multimodal with macropores (~1.8-1.9 nm), smaller (~2.1-2.3 nm) and larger (~13.1nm) mesopores. For Bi_2WO_6 (S1), the PSD curve is trimodal with smaller (~2.0-2.4 nm) mesopores and larger (~13.1 nm) mesopores. The BET

surface area of the Bi_2WO_6 (S1), Bi_2WO_6/BiOCl (S2) and BiOCl (S3) are 13.64, 16.88 and 40.73 m^2/g, respectively. Above results clearly suggest that Bi_2WO_6/BiOCl (S2) has the larger specific surface area and pore volume. Thus, the Bi_2WO_6/BiOCl (S2) would be favorable for dye molecules adsorption and makes the transport of reactants easier, which may improve its photocatalytic activity.

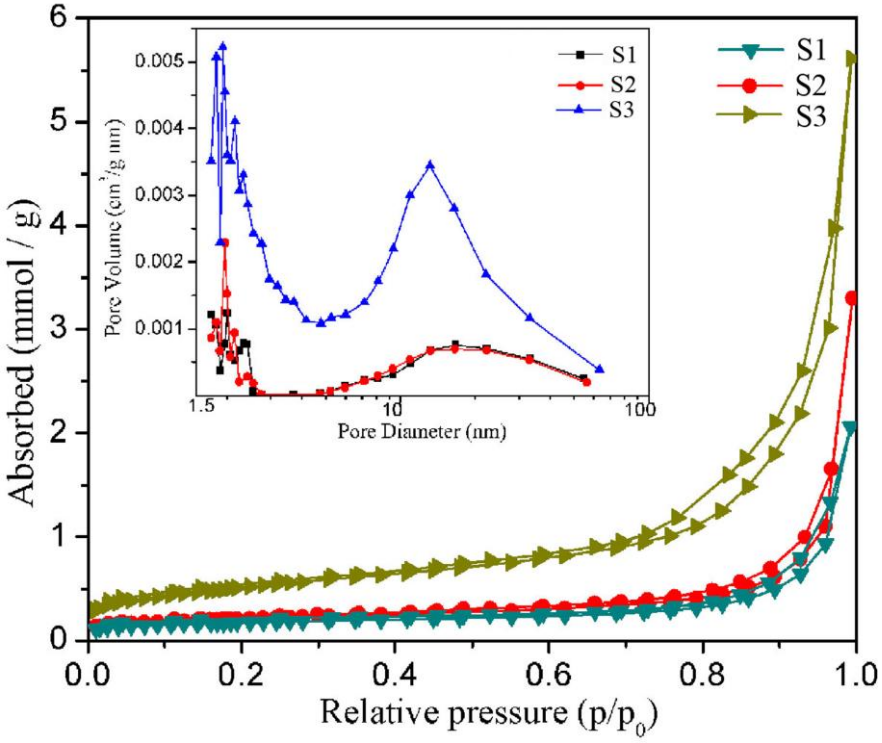

Fig. 8

3.7. Photocatalytic studies

The photocatalytic activities of the as-prepared samples were measured by the degradation of DNP in water under the irradiation of visible light (Xe-lamp, 300 W). Fig. 9 presents the UV-vis absorption spectra of DNP solution at different visible light illumination times. The decrease of the characteristic absorption of DNP at a wavelength of 360 nm would imply decrease of 2,4-DNP content. The absorption at 360 nm over an aqueous solution of 2,4-DNP, which decreased after stirring for 30 min in the dark, indicates that the 2,4-DNP was adsorbed on the photocatalyst. It can be easily seen that for sample S2, the intensity of absorption peak at 360 nm decreased drastically over time, and completely disappeared after visible light illumination for 30

min. This indicated that sample S2 has the highest activity for degradation of DNP.

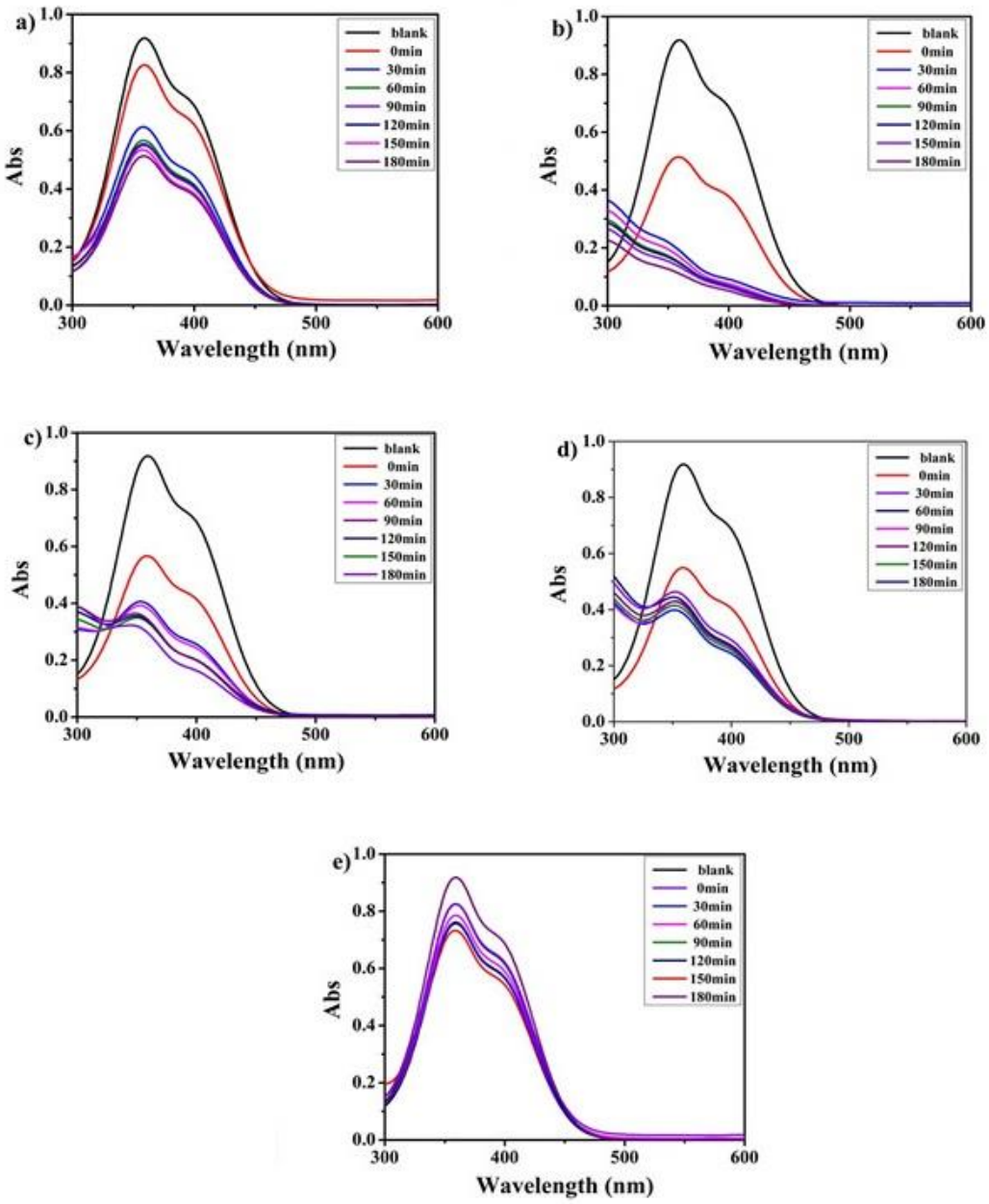

Fig. 9

The photocatalytic degradation curves of DNP as a function of time is depicted in Fig. 10. As shown in Fig. 10, the blank experiment suggested that the photolysis of DNP is negligible under visible irradiation. After visible light illumination for 30 min, the degradation efficiency of DNP is 33.25% (S1), 79.08% (S2), 56.69% (S3), 50.81% (S4) and 11.5% (S5), respectively. When pure Bi_2WO_6 (S1) and pure BiOCl (S3) was used, the photocatalytic activity is

a bit low for degradation of DNP. However, the $BiOCl/Bi_2WO_6$ heterojunctions (S2) exhibit much better photocatalytic activity than pure BiOCl and Bi_2WO_6 photocatalyst. The results demonstrate that the formation of the $BiOCl/Bi_2WO_6$ heterojunctions is crucial for enhancing photocatalytic performance. Besides, When $BiOCl/Bi_2WO_6$ synthesized without ultrasonic treatment was used as the photocatalyst, the photodegradation of DNP is obviously worse than that by $BiOCl/Bi_2WO_6$ prepared via ultrasonic route. The situation is similar for $BiOCl/Bi_2WO_6$ photocatalyst fabricated by using KCl (S5) as the chlorine source. The photocatalytic activity of S5 is much lower than that of $BiOCl/Bi_2WO_6$ fabricated by using [BMIM]Cl (S2) as the chlorine source. This is because of the crystallinity (as shown in Fig. 2) and the formation of the heterojunction. On the one hand, a high degree of crystallinity is considered essential to enhance the photocatalytic activity of a given material [46]. Obviously, the degree of crystallinity for S2 is much higher than S4 (Fig. 2), which leads to the higher photocatalytic activity of S2. On the other hand, the formation of the heterojunction can facilitate charge/hole transfers between the tungstate and chloride and promote the electron-hole pair separations during the photocatalytic processes, this is beneficial for the enhancement of the photocatalytic activity. Thus, the photocatalytic activity of S2 ($BiOCl/Bi_2WO_6$ heterojunctions) is higher than S4 (BiOCl).

To quantitatively compare the photocatalytic abilities of the as-prepared samples, the photocatalytic degradation kinetics of DNP was investigated, as show in Fig. 10b. The rate constant values of DNP degradation were calculated to be 0.0042 min^{-1}, 0.0155 min^{-1}, 0.0083min^{-1}, 0.0066 min^{-1} and 0.0016 min^{-1} for sample S1, S2, S3, S4 and S5, respectively. It can be seen that the degradation rate of S2 is bigger than other samples. It can be concluded that $BiOCl/Bi_2WO_6$ synthesized via an ionic liquid assisted ultrasound method (S2) exhibited superior photocatalytic activity, which is attributed to the high degree of crystallinity and the formation of the heterojunction.

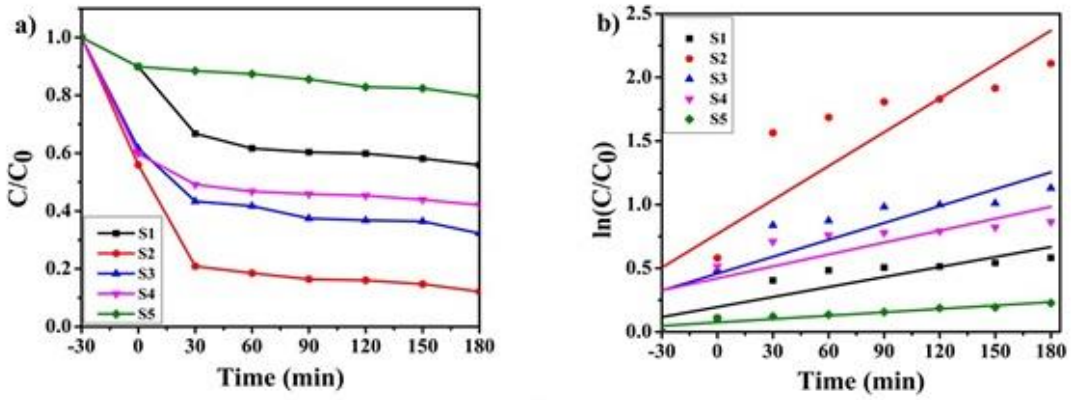

Fig. 10

Besides degradation of the colorless dye, we also did the experiment of the photocatalytic performance on the obtained photocatalysts for degrading RhB and QB. Fig. 11a presents the variation of RhB concentration (C/C_0) as the function of reaction time. As shown in Fig. 11a, after visible light irradiation for 100 min, the photodegradation efficiencies of RhB are 47%, 99%, 98%, 83% and 17% for S1, S2, S3, S4 and S5, respectively. As a comparison, only about 3% RhB was degraded without photocatalyst under the same conditions (blank experiment), which indicates that the self-photolysis of RhB is very limited and can be negligible. To quantitatively compare the photocatalytic abilities of the as-prepared samples, the photocatalytic degradation kinetics of RhB was investigated, as show in Fig. 11b. The rate constant values of RhB degradation were calculated to 0.0032 min^{-1}, 0.0382 min^{-1}, 0.0270min^{-1}, 0.0105 min^{-1} and 0.0002 min^{-1} for sample S1, S2, S3, S4 and S5, respectively, indicating that S2 shows the highest photocatalytic ability. It is observed from Fig. 11 c that the characteristic absorption peak of RhB is shown at 553 nm. With the illumination time increasing, the concentration of RhB continuously decreases and the peak of RhB is apparently blue-shifted, such a shift indicates that RhB was degraded to other small molecules.

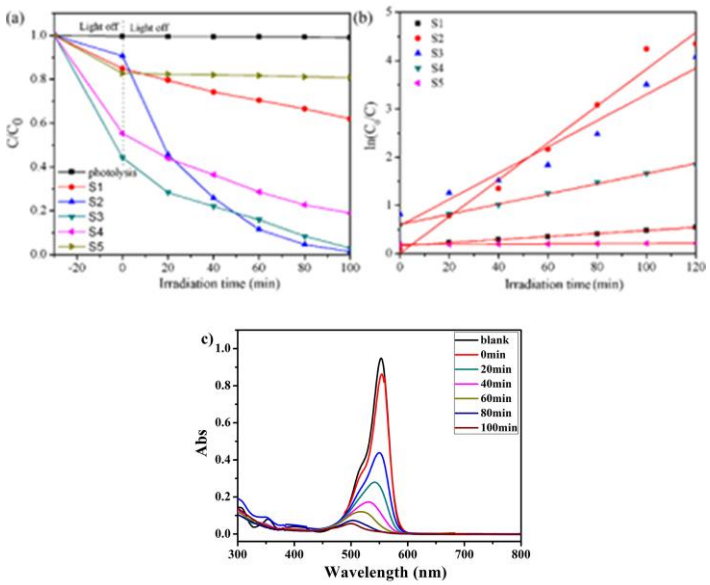

Fig. 11

Quinoline blue (QB) was also used to test the photocatalytic activities of the above samples obtained via the ionic liquid assisted ultrasonic method (Fig. 12). After irradiation for 120 min under visible light, the photodegradation efficiencies for QB are about 10%, 97%, 32%, 41% and 2% for sample S1, S2, S3, S4 and S5, respectively. The rate constant values of QB degradation were calculated to 0.0006 min^{-1}, 0.0217 min^{-1}, 0.0009 min^{-1}, 0.0026 min^{-1} and 0.0001 min^{-1} for sample S1, S2, S3, S4 and S5, respectively. All results clearly indicate that the as-prepared Bi_2WO_6/BiOCl (S2) heterojunction shows the highest photocatalytic activity. The UV-vis absorption spectra of QB solution at different visible light irradiation times is presented in Fig. 12 c. It can be seen that the absorption peak of QB (at 638 nm) decreases and is blue-shifted in the spectra with the visible light irradiation time. This suggests that QB is degraded to other small molecules and the decrease of the QB concentration is due to photocatalytic degradation rather than physical adsorptions.

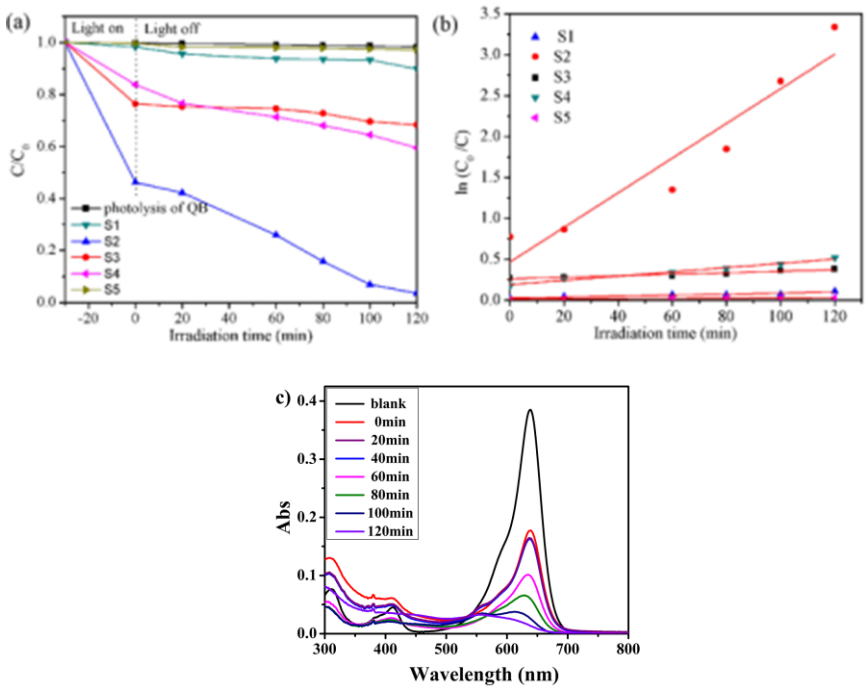

Fig. 12

Sunlight is inexhaustible, renewable and free energy, so the investigation of degradation under sunlight is much desired and has a great significant effect on both resource and environment. Herein, the degradation of RhB and QB with the as-prepared samples was investigated under the sunlight irradiation at room temperature. Figure 13 c shows the degradation curves of RhB on S2 under sunlight illumination. It can be clearly seen that RhB is decomposed by about 50% within 30 min in the solution of BiOCl/Bi_2WO_6 heterostructures and is almost completely decomposed after 120 min. Fig. 13a shows the results of photocatalytic degradation of QB solution under sunlight irradiation, where it can be seen that QB was completely degraded with Bi_2WO_6 (S1), and Bi_2WO_6/BiOCl (S2) in 120 min. The rate constant values of QB with Bi_2WO_6 (S1), Bi_2WO_6/BiOCl (S2), and BiOCl (S3) are 0.025 min^{-1}, 0.034 min^{-1}, and 0.006 min^{-1}, respectively, indicating the higher degradation rates under sunlight irradiation than those under visible light (Fig. 13b).

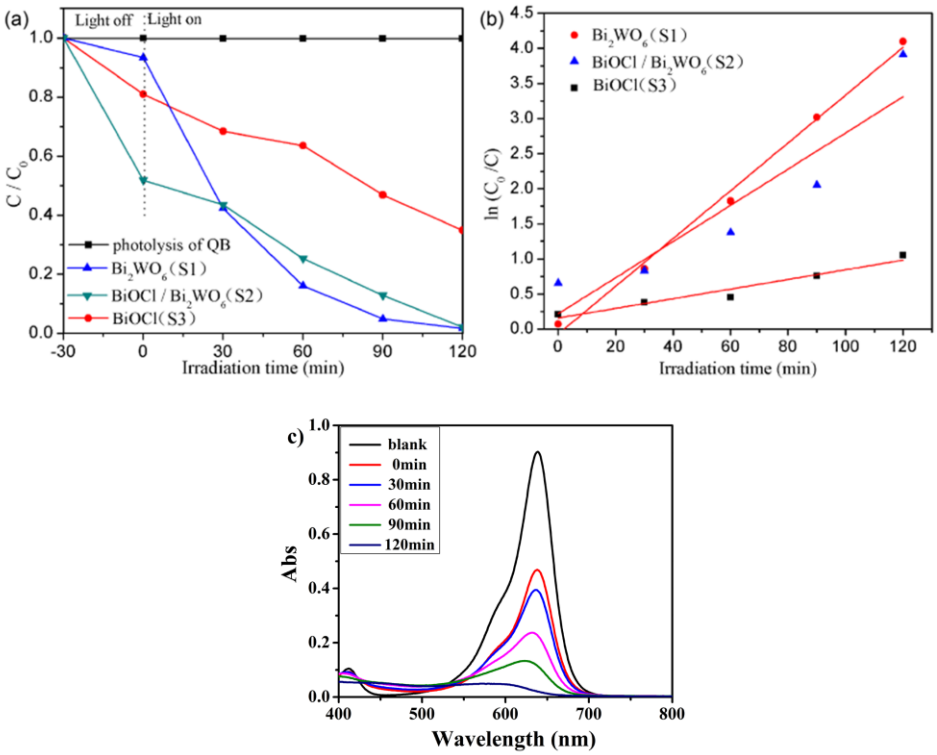

Fig. 13

The similar results were also observed in the degradation of RhB under the same conditions (Fig. 14). These results demonstrate that the sunlight can act as an available light source for the photocatalytic degradation of dyes.

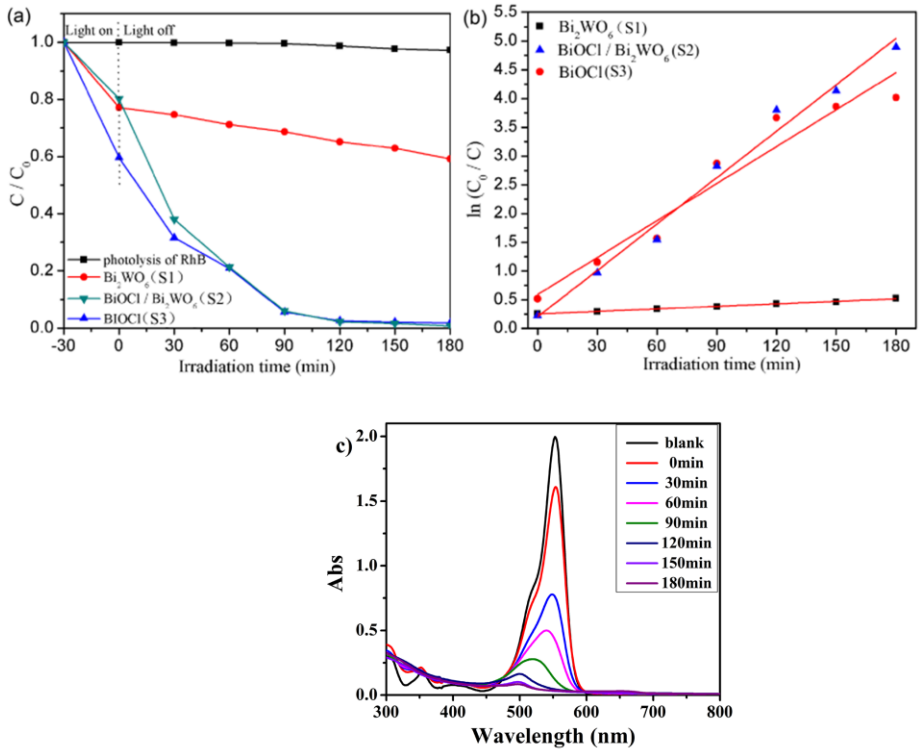

Fig. 14

To observe the stability of as-prepared Bi_2WO_6/BiOCl heterojunction (S2) under light irradiation, the recycling experiments were conducted to degrade RhB under visible light irradiation. As shown in Fig. 15, the photodegradation efficiency of RhB decreases from 98% to 91.7% at 120 min after four runs. It indicates that the as-prepared Bi_2WO_6/BiOCl heterojunction (S2) is stable under visible light irradiation.

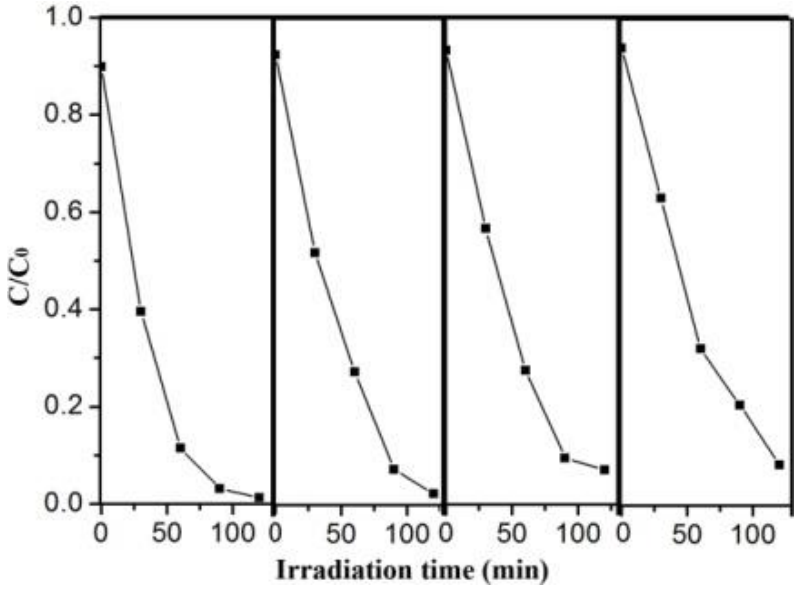

Fig. 15

3.8. Band structures

To explore electronic structures of the systems, the formation structure of the heterojunction is studied beforehand. In the present systems, the Bi_2WO_6/BiOCl complexes are composed of three parts, Bi_2WO_6–Interface–BiOCl. Crystal structures of the tungstate and chloride can be performed experimentally e.g., through the HRTEM in Fig. 5. The optimized supercell structures of the pristine Bi_2WO_6, BiOCl, and the Bi_2WO_6/BiOCl heterojunction are depicted on the upper sides of Fig. 16 (a). The calculated band structures are depicted on the bottom sides of Fig. 16 (b)-(d) for the bulk Bi_2WO_6, BiOCl and the Bi_2WO_6/BiOCl heterojunction, respectively. The band gaps for the bulks are 1.86 and 2.78 eV for the Bi_2WO_6 and BiOCl, as denoted by grey arrows in the figures. The theoretical values though in good agreements with previous theoretical results [47, 48], are systematically lower than the experimental

values in Fig. 7. This is a well-known reason due to the GGA approximations which typically underestimate the gap energy as a result of compromise between computational efficiencies and accuracies.

The band structure of Bi_2WO_6/BiOCl heterojunction is different from these of the bulk counterparts. Fig. 16 (d) shows the calculated results where the same high-symmetry points as these for the bulk BiOCl are employed here. Comparing with the structures of pure Bi_2WO_6 and BiOCl, the bands drawn in green lines next to the conduction band minimum (CBM) of the heterojunction are mainly consisted of the bands arising from the BiOCl. They lies below the bands from the tungstate (shown in purple lines) with a maximum offset value of 0.87 eV. On the other hand, bands next to the valence band maximum (VBM) of the heterojunction is mainly composed of the bands from the Bi_2WO_6. They are depicted as blue lines. Interestingly, two additional lines were found crossing the Fermi level. They are a green line contributed from BiOCl above a pink line from the Bi_2WO_6. The maximum vertical discrepancy between the lines is 0.21 eV next to the M point. These two bands act as tangling bands, through where electrons can move freely [49]. The intercalation of the bands from two parts make the heterojunction's band structure different from their bulk counterparts. The bands have a gap value of 1.14 eV with an indirect bandgap nature.

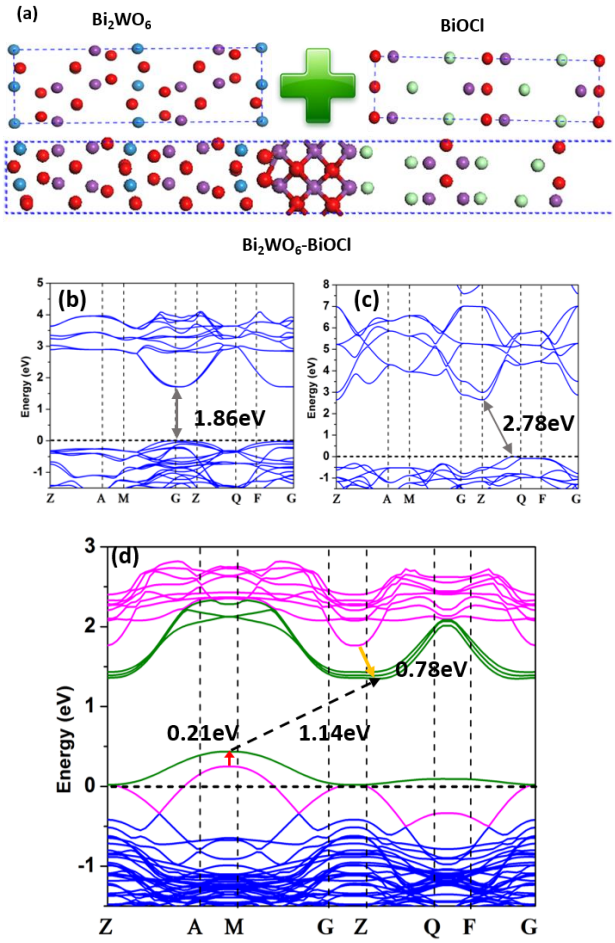

Fig. 16

3.9. Photocatalytic mechanism

The possible photocatalytic mechanism of the degradation of DNP with Bi_2WO_6/BiOCl heterojunction (S2) as a model under visible light irradiation was investigated. Various scavengers were introduced to react with active species to evaluate their contributions on the photodegradation (Fig. 17). It is well known that benzoquinone (BQ) [50] and tertiary butanol (t-BuOH) [51] are the effective traps for $\bullet O_2^-$ and •OH, respectively. As shown in Fig. 17, the addition of BQ and t-BuOH suppressed the degradation of DNP, indicating that $\bullet O_2^-$ and •OH play important roles in the degradation reaction. When potassium iodide (a scavenger for h^+) [52] was added, the photodegradation rate was almost not changed, suggesting that h^+ can be negligible in the photocatalytic process. These results indicate that $\bullet O_2^-$ and •OH play more important roles than hole in the degradation of DNP.

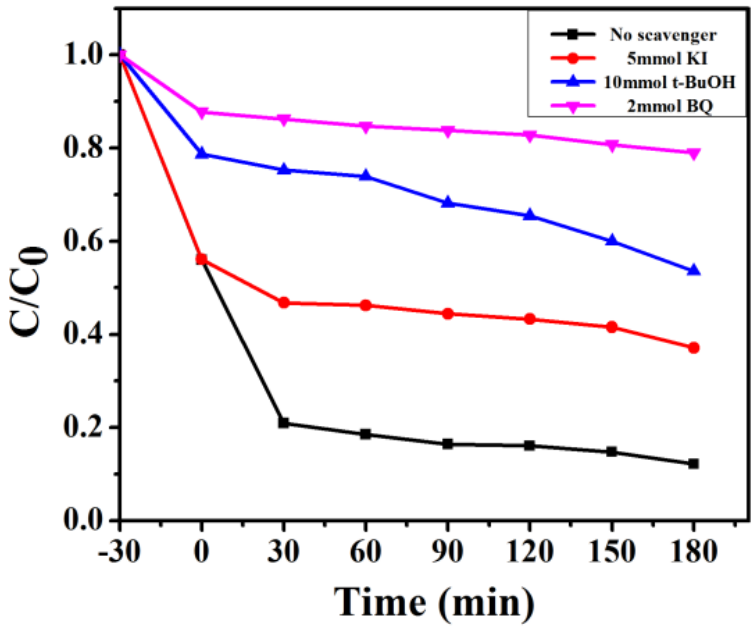

Fig. 17

It is well known that the migration direction of the photo-generated charge depends on the band structure of semiconductors. In order to investigate the effect of band structure of the Bi_2WO_6/BiOCl samples, the potentials of conduction bands (CB) of Bi_2WO_6 and BiOCl are calculated by Mulliken electronegativity theory: $E_{VB} = X - E_e + 0.5 * E_g$, where X is defined as the geometric mean of the absolute electronegativity of the constituent atoms and E_e is the energy of free electrons on the hydrogen scale (4.5 eV). Eg is the VB edge potential and the band gap of the semiconductor. The potentials of valence band (VB) edges can be calculated by $E_{CB} = E_{VB} - E_g$. Therefore, according to the above equations, the E_{VB} values and the E_{CB} of Bi_2WO_6 were calculated to be 3.33 eV and 0.45 eV, respectively; For BiOCl, they were estimated to be 3.32 eV and 0.39 eV, respectively.

Based on the above experimental and first-principles results, a possible photocatalytic mechanism for the degradation of pollutants under visible light irradiation was proposed (Fig. 18). Under the irradiation of visible light, electrons (e^-) from VB of the Bi_2WO_6 were excited to CB, leaving to the same amount of holes (h^+) VB. As denoted in the red arrow in Fig. 16 (d), the holes are able to pop up through the dangling bands crossing the Fermi-level, and

pass the interface to the BiOCl side. On the other hand, the photoexcited electrons of the Bi_2WO_6 part will firstly reach the CBs of its own, then cross the interfacial region to the energetically lower CBs featured as BiClO electronic structures (green lines next to CBM at Fig. 16 (d)). The part was drawn as orange arrow in the figure. It is noteworthy that the hole migration is highly probable in the k-space since two bands are aligned in the same position as shown Fig 16 (d). Similarly, the photoexited electrons also have feasible transition channels due to the band minimums aligning very closely to the same symmetric Z point in k-space. Furthermore, recombination through indirect band would require participation from other factors (e.g. phonons) to satisfy conservation of momentum. Thus, electron-hole recombination efficiency is very low at the interfacial region. Consequentially, the band intercalation of the heterojunction can substantially delay recombination between photoinduced electrons and holes. Later, the photo-generated electrons were captured by O_2 to yield $\bullet O_2^-$ and H_2O_2. At the same time, •OH can be obtained from H_2O_2 or OH^- in the presence of holes. At last, •OH and $\bullet O_2^-$ react with dyes, and induce the decomposition of the dyes.

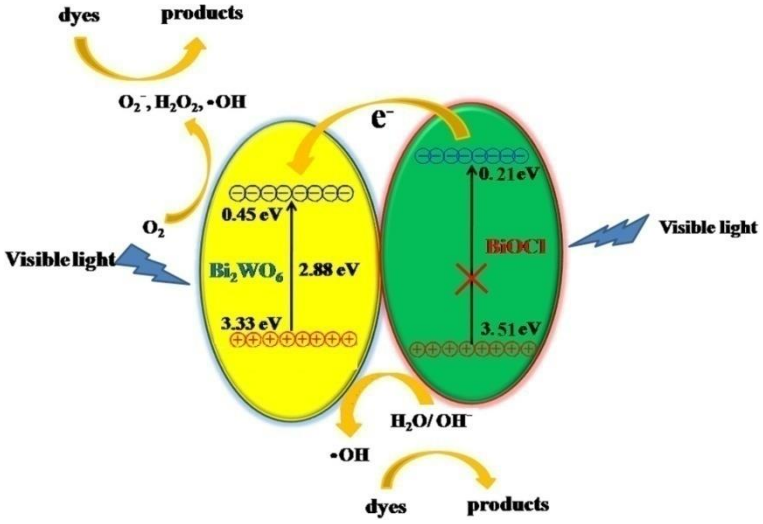

Fig. 18

3.10. Photocurrent Properties

Photocurrent properties were also determined for the synthetic samples. Transient photocurrent measurements were performed by placing the as-prepared

BiOCl, Bi_2WO_6 and BiOCl-Bi_2WO_6 on electrodes during repeated ON/OFF sunlight irradiation cycles. As shown in Fig. 19, the photocurrent does not reach equilibrium at first. After about 200 seconds, the photocurrent value becomes stable when the incident light on the photoanode is turned off and retracts to the original value once the light is turned on again. These samples generate photocurrent density with a repeated response to on/off cycles under pulsed interval irradiation, demonstrating that the photoanodes are stable. Besides, the BiOCl-Bi_2WO_6 heterojunction exhibited a higher transient photocurrent density (about 0.16 μA) than those of the Bi_2WO_6 sample (0.15 μA) and the BiOCl sample (0.1 μA). Similar to the mechanism leading to enhanced photocatalytic abilities, intercalations of indirect band at the BiOCl-Bi_2WO_6 heterojunction region prompt separations of negative and positive charges, resulting in enhanced photocurrent at the heterojunctions. Consequently, recombination of the electron and holes is inhibited in the photo processes. The conclusion is in line with photocatalytic mechanism as proposed above.

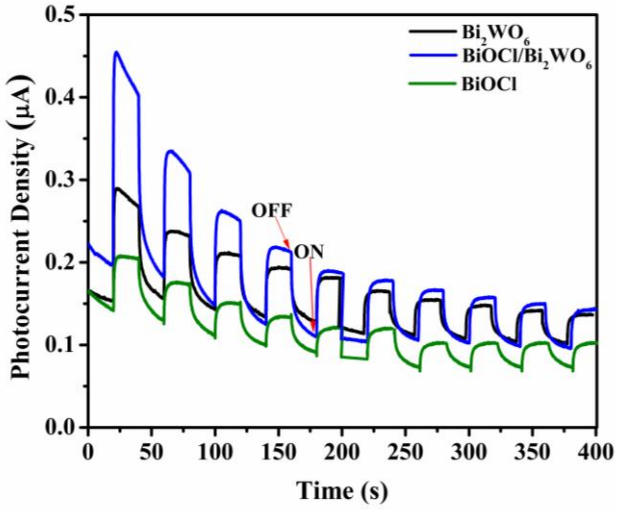

Fig. 19

4. Conclusion

In summary, Bi_2WO_6/BiOCl heterojunction has been successfully synthesized via a facile one-step process of the ionic-liquid assisted ultrasonic irradiation at room temperature. The formation of heterojunction structures was confirmed by XRD and SEM. The results suggest that the amount of the [BMIM]Cl has a significant influence on the structures. Compared with BiOCl

and Bi_2WO_6, the prepared Bi_2WO_6/BiOCl heterojunction has high photocatalytic activities for the degradation of organic dyes under the visible light and sunlight irradiation. Through experimental determinations and first-principles computations, intercalations of indirect band at the heterojunction region were found to facilitate charge/hole transfers between the tungstate and chloride, promoting the electron-hole pair separations during the photocatalytic processes. Such a mechanism is further verified in the photocurrent measurement where the heterojunction has higher photocurrent property. Therefore, the Bi_2WO_6/BiOCl heterojunction is expected to have wide applications in organic pollutant removal.

Acknowledgements

The authors acknowledge with thanks the financial support of the National Natural Science Foundation of China (21343008; 21601149) and Scientific Research Fund of Hunan Provincial Education Department, China (16B253), the Open Project Program of State Key Laboratory of Structural Chemistry, China (No. 20150018) and Hunan 2011 Collaborative Innovation Center of Chemical Engineering & Technology with Environmental Benignity and Effective Resource Utilization and the Oulu University Strategic Grant. T. Li acknowledges Oulu University Short-term International Research Visit grant during his stay in Finland. Author Meng Zhang thanks Dr. Wenjuan Yang at Huazhong University of Science and Technology for her useful discussion.

References

[1] H. L. Lin, J. Cao, B. D. Luo, B.Y. Yan, S. F. Chen, Visible-light photocatalytic activity and mechanism of novel AgBr/BiOBr prepared by deposition-precipitation, Chin. Sci. Bull. 57 (2012) 2901.

[2] L. Chen, S. F. Yin, S. L. Luo, R. Huang, Q. Zhang, T.Hong, C. T. Peter, $Bi_2O_2CO_3$/BiOI photocatalysts with heterojunctions highly efficient for visible-light treatment of dye-containing wastewater, Ind. Eng. Chem. Res. 51 (2012) 6760.

[3] M. G. Walter, E. L. Warren, J. R.Mckone, S. W. Boettcher, Q. X. Mi, E. A. Santori, N. S. Lewis, Solar water splitting cells, Chem. Rev. 110 (2010) 6446.

[4] J. H. Xu, W. Z. Wang, S. M. Sun, L Wang, Enhancing visible-light-induced photocatalytic activity by coupling with wide-band-gap semiconductor: A case study on Bi_2WO_6/TiO_2, Appl. Catal., B 111 (2012) 126.

[5] J. Y Sheng, X. J. Li, Y. M. Xu, Generation of H_2O_2 and OH radicals on Bi_2WO_6 for phenol degradation under visible light, ACS Catal. 4 (2014) 732.

[6] Q. C. Xu, D. V. Wellia, Y. H. Ng, R. Amal, T. T. Y.Tan, Synthesis of porous and visible-light absorbing Bi_2WO_6/TiO_2 heterojunction films with improved photoelectrochemical and photocatalytic performances, J. Phys. Chem. C 115 (2011) 7419.

[7] C. Zhang, Y. F. Zhu, Synthesis of square Bi_2WO_6 nanoplates as high-activity visible-light-driven photocatalysts, Chem. Mater. 17 (2005) 3537.

[8] Y. Yan, Y. F. Wu, Y. T. Yan, W.S. Guan, W. D. Shi, Inorganic-salt-assisted morphological evolution and visible-light-driven photocatalytic performance of Bi_2WO_6 nanostructures, J. Phys. Chem. C 117 (2013) 20017.

[9] M. Shang, W. Wang, L. Zhang, S.Sun, L.Wang, L.J. Zhou, 3D Bi_2WO_6/TiO_2 hierarchical heterostructure: controllable synthesis and enhanced visible photocatalytic degradation performances, Phys. Chem. C 113 (2009) 14727.

[10] Z. J. Zhang, W. Z. Wang, L. Wang, S. M. Sun, Enhancement of visible-light photocatalysis by coupling with narrow-band-gap semiconductor: a case study on Bi_2S_3/Bi_2WO_6, ACS Appl. Mater. Interfaces 4 (2012) 593.

[11] D. Q. He, L. L. Wang, D. D. Xu, J. L. Zhai, D. J. Wang, T. F. Xie, Investigation of photocatalytic activities over $Bi_2WO_6/ZnWO_4$ composite under UV light and its photoinduced charge transfer properties, ACS Appl. Mater. Interfaces 3 (2011) 3167.

[12] Y. D. Guo, G. K. Zhang, J. Liu, Y. L. Zhang, Hierarchically structured α-Fe_2O_3/Bi_2WO_6 composite for photocatalytic degradation of organic contaminants under visible light irradiation, RSC Adv. 3 (2013) 2963.

[13] M. S. Gui, W. D. Zhang, Y. Q. Chang, One-step hydrothermal preparation strategy for nanostructured WO_3/Bi_2WO_6 heterojunction with high visible light photocatalytic activity, Chem. Eng. J. 197 (2012) 283.

[14] G. Colón, S. M. López, M. C. Hidalgo, Sunlight highly photoactive Bi_2WO_6–TiO_2 heterostructures for rhodamine B degradation, J. A. Navío. Chem. Commun. 46 (2010) 4809.

[15] J.Q. Li, Z. Y. Guo, Y. Wang, Z. F. Zhu, Three-dimensional TiO_2/Bi_2WO_6 hierarchical heterostructure with enhanced visible photocatalytic activity, Micro & Nano Lett. 9 (2014) 65.

[16] M. Ge, Y. Li, L. Liu, Z. Zhou, W. Chen, Preparation and visible light photocatalytic activity of Bi_2O_3/Bi_2WO_6 heterojunction photocatalysts, J. Phys. Chem. C 115 (2011) 5220.

[17] J. X. Xia, J. Di; S, Yin; H. Xu, J. Zhang, Y. G. Xu, L Xu, H. M. Li, M. G. Xia, Facile fabrication of the visible-light-driven Bi_2WO_6/BiOBr composite with enhanced photocatalytic activity, RSC Adv. 4 (2014) 82.

[18] L. P. Zhu, G. H. Liao, N. C Bing, Self-assembled 3D BiOCl hierarchitectures: tunable synthesis and characterization, CrystEngComm 12 (2010) 3791.

[19] X. Zhang, Z. H. Ai, F. L. Jia, L. Z. Zhang, Generalized one-pot synthesis, characterization, and photocatalytic activity of hierarchical BiOX (X= Cl, Br, I) nanoplate microspheres, J. Phys. Chem. C 112 (2008) 747.

[20] L.Q. Ye, L. Zan, L.H. Tian, T.Y. Peng, J. J. Zhang, The {001} facets-dependent high photoactivity of BiOCl nanosheets, Chem. Commun. 47 (2011) 6951.

[21] W. J. Yang, B. Ma, W. C. Wang, Y. W. Wen, D. W. Zeng, B. Shan, Enhanced photosensitized activity of a BiOCl–Bi_2WO_6 heterojunction by effective interfacial charge transfer, Phys. Chem. Chem. Phys 15 (2013) 19387.

[22] W.B. McNamara, Y.T. Didenko, K.S. Suslick, Pressure during sonoluminescence, J. Phys. Chem. B 107 (2003) 7303.

[23] N.A. Dhas, A. Ekhtiarzadeh, K.S. Suslick, Sonochemical preparation of supported hydrodesulfurization catalysts, J. Am. Chem. Soc. 123 (2001) 8310.

[24] Z. Ma, J. H. Yu, S. Dai, Preparation of inorganic materials using ionic liquids, Adv. Mater. 22 (2010) 261.

[25] M. Antonietti, D. B. Kuang, B. Smarsly, Y. Zhou, Ionic liquids and microwaves-making zeolites for emerging applications, Angew. Chem. Int. Ed. 43 (2008) 4988.

[26] J. A. Dahl, B. L. S. Maddux, J. E. Hutchison, Toward greener nanosynthesis, Chem. Rev. 107 (2007) 2228.

[27] F. T. Li, Q. Wang, X. J. Wang, B. Li, Y. J. Hao, R.H. Liu, D. S. Zhao, In-situ one-step synthesis of novel BiOCl/$Bi_{24}O_{31}Cl_{10}$ heterojunctions via self-combustion of ionic liquid with enhanced visible-light photocatalytic activities, Appl. Catal. B 150 (2014) 574.

[28] J. Zhang, J. X. Xia, S. Yin, H. M. Li, H. Xu, M. Q. He, L.Y. Huang, Q. Zhang, Improvement of visible light photocatalytic activity over flower-like BiOCl/BiOBr microspheres synthesized by reactable ionic liquids, Colloids Surf. A 420 (2013) 89.

[29] X. J. Wang, Q. Wang, F. T. Li, W. Y. Yang, Y. Zhao, Y. J. Hao, S. J. Liu, Novel BiOCl–C_3N_4 heterojunction photocatalysts: In situ preparation via an ionic-liquid-assisted solvent-thermal route and their visible-light photocatalytic activities, Chem. Eng. J. 234 (2013) 361.

[30] J. X. Xia, L. Xu, J. Zhang, S. Yin, H. M. Li, H. Xu, J. Di, Improved visible light photocatalytic properties of Fe/BiOCl microspheres synthesized via self-doped reactable ionic liquids, CrystEngComm 15 (2013) 10132.

[31] J. Di, J. X. Xia, S. Yin, S. Yin, H. Xu, M.Q. He, H. M. Li, L.Xu, Y.P. Jang, AgC_3N_4/BiOBr visible-light-driven composite: synthesis via a reactable ionic liquid and improved photocatalytic activity, RSC Adv. 3 (2013) 19624.

[32] H. Bu, M. Zhao, H. Zhang, X. Wang, Y. Xi, Z. Wang, Isoelectronic doping of graphdiyne with boron and nitrogen: stable configurations and band gap modification, J. Phys. Chem. A 116 (2012) 3934–3939.

[33] J.P. Perdew, K. Burke, M. Ernzerhof, Generalized gradient approximation made simple, Phys. Rev. Lett. 77 (1996) 3865–3868.

[34] E. Keller, V. Krämer, A Strong Deviation from Vegard's Rule: X-Ray Powder Investigations of the Three Quasi-Binary Phase Systems BiOX–BiOY (X, Y = Cl, Br, I), Z. für. Naturforsch B 60 (2005) 1255.

[35] N. A. McDowell, K. S. Knight, Philip Lightfoot, Unusual High-Temperature Structural Behaviour in Ferroelectric Bi_2WO_6, Chemistry–A European Journal 5 (2006) 1493-1499.

[36] W. C. Wang, W. J. Yang, R. Chen, X. B. Duan, Y. L. Tian, D. W. Zeng, B. Shan, Investigation of band offsets of interface BiOCl:Bi_2WO_6: a first-principles study, Phys. Chem. Chem. Phys. 14 (2012) 2450–2454.

[37] J. H. Ryu, S. Y. Bang, W. S. Kim, G. S. Park, K. M. Kim, J. W. Yoon, K. B. Shim, N. Koshizaki, Microstructure and optical properties of nanocrystalline $CaWO_4$ thin films deposited by pulsed laser ablation in room temperature, J. Alloys Compd. 411 (2007) 146.

[38] O. Lupan, L. Chow, L. K. Ono, B. R. Cuenya, G. Y. Chai, H. Khallaf, S. Park, A. Schulte, Synthesis and characterization of Ag-or Sb-doped ZnO nanorods by a facile hydrothermal route, J. Phys. Chem. C 114 (2010) 12401.

[39] F. Dong, Y. J. Sun, M. Fu, Z. B. Wu, S. C. Lee, Room temperature synthesis and highly enhanced visible light photocatalytic activity of porous BiOI/BiOCl composites nanoplates microflowers, J. Hazard. Mater. 219 (2012) 26.

[40] H. Q. Jiang, M. Nagai, K. Kobayashi, Enhanced photocatalytic activity for degradation of methylene blue over V_2O_5/$BiVO_4$ composite, J. Alloys Compd. 479 (2009) 821.

[41] X. Zhang, Z. H. Ai, F. L. Jia, L. Z. Zhang, Generalized one-pot synthesis, characterization, and photocatalytic activity of hierarchical BiOX (X= Cl, Br, I) nanoplate microspheres, J. Phys. Chem. C 112 (2008) 747.

[42] J. Wu, J. F. Duan, Y. Zheng, Y. Xie, Synthesis of Bi_2WO_6 nanoplate-built hierarchical nest-like structures with visible-light-induced photocatalytic activity, J. Phys. Chem. C 111 (2007) 12866.

[43] J. Q. Liu, J. J. Hu, L. L. Ruan, Y.C. Wu, Facile and environment friendly synthesis of hierarchical BiOCl flowery microspheres with remarkable photocatalytic properties, Chin. Sci. Bull. 59 (2014) 802.

[44] X. C. Wang, J. C. Yu, Y. L. Chen, L. Wu, X. Z. Fu, ZrO2-Modified Mesoporous Nanocrystalline TiO_2-xN_x as Efficient Visible Light Photocatalysts, Environ. Sci. Technol. 40 (2006) 2369.

[45] L. P. Zhu, G. H. Liao, N. C. Bing, Self-assembled 3D BiOCl hierarchitectures: tunable synthesis and characterization, CrystEngComm 12 (2010) 3791.

[46] A. E. Maegli, T. Hisatomi, E. H. Otal, S. Yoon, S. Pokrant, Structural and photocatalytic properties of perovskite-type (La,Ca)Ti(O,N)$_3$ prepared from A-site deficient precursors, J. Mater. Chem. 22 (2012) 17906-17913.

[47] H. B. Fu, C. Pan, W. Q. Yao, Y. F. Zhu, Visible-Light-Induced Degradation of Rhodamine B by Nanosized Bi_2WO_6, J. Phys. Chem. B 109 (2005) 22432-22439.

[48] K. L. Zhang, C. M. Liu, F. Q. Huang, C. Zheng, W. D. Wang, Study of the electronic structure and photocatalytic activity of the BiOCl photocatalyst, Appl. Catal. B 68 (2006) 125-129.

[49] W. J. Yang, Y. W. Wen, D. W. Zeng, H. Yy, Interfacial Charge Transfer and Enhanced Photocatalytic Performance for the Heterojunction WO_3/BiOCl: First Principles Study, J. Mater. Chem. A 2 (2014) 20770-20775.

[50] S. W. Zhu, Q. G. Li, F. Li, W. Cao, T. H. Li, One-pot synthesis of Ag^+ doped $BiVO_4$ microspheres with enhanced photocatalytic activity via a facile hydrothermal method, J. Phys. Chem. Solids 92 (2016) 16.

[51] S. W. Zhu, Q. G. Li, T. H. Li, W. Cao, M. Huttula, One-pot hydrothermal synthesis of $BiVO_4$ microspheres with mixed crystal phase and Sm^{3+}-doped $BiVO_4$ for enhanced photocatalytic activity, J. Mater. Sci. 52 (2017) 1679-1693.

[52] S. Song, L. J. Xu, Z. Q. He, J. M. Chen, X. Z. Xiao, Mechanism of the photocatalytic degradation of CI Reactive Black 5 at pH 12.0 using $SrTiO_3$/CeO_2 as the catalyst, Environ. Sci. Technol. 41 (2007) 5846.

Table and Figure captions

Table 1 The synthetic conditions of Bi_2WO_6/BiOCl composites

Fig. 1 XRD patterns of (a) BiOCl (S3), (b) Bi_2WO_6/BiOCl (S2) and (c) Bi_2WO_6 (S1).

Fig. 2 XRD patterns of (a) S4 and (b) S5.

Fig. 3 FT-IR spectrum of (a) Sample S2 and (b) pure [BMIM]Cl.

Fig. 4 SEM images of as-prepared samples (a) Bi_2WO_6 (S1), (b) BiOCl (S3) (c) the low magnification SEM image with Bi_2WO_6/BiOCl (S2), (d) the high magnification SEM image of Bi_2WO_6/BiOCl (S2).

Fig. 5 TEM images (a, b) and HETEM images (c, d) of Bi_2WO_6/BiOCl (S2)

Fig. 6 (a) Whole XPS spectrum pattern of the Bi_2WO_6/BiOCl (S2) heterojunction (b) W4f of Bi_2WO_6/BiOCl (S2), (c) O1s of Bi_2WO_6/BiOCl (S2), (d) Cl2p of Bi_2WO_6/BiOCl (S2), (e) Bi4f of Bi_2WO_6/BiOCl. (f) EDS of the Bi_2WO_6/BiOCl (S2).

Fig. 7 UV-Vis diffuse reflectance absorption spectra for the as-prepared samples. The inset shows the band gap value estimated from a plot of $(\alpha h\nu)^{1/2}$ versus photon energy.

Fig. 8 Nitrogen adsorption–desorption isotherm and pore size distribution (inset) for the as-prepared samples.

Fig. 9 UV-vis absorption spectrum of the DNP solution (10 mg/L) in the presence of (a) S1; (b) S2; (c) S3; (d) S4; (e) S5 under visible light illumination.

Fig. 10 Time-course variation of (a) C/C_0 and (b) ln(C_0/C) of DNP solution under visible light irradiation over various catalysts.

Fig. 11 Time-course variation of (a) C/C_0 and (b) ln(C_0/C) of RhB solution under visible light irradiation over various catalysts; (c) UV-vis absorption spectrum of the RhB solution in the presence of S2.

Fig. 12 Time-course variation of (a) C/C_0 and (b) ln(C_0/C) of QB solution under visible light irradiation over various catalysts; (c) UV-vis absorption spectrum of the QB solution in the presence of S2.

Fig. 13 (a) Time-course variation of (a) C/C_0 and (b) $\ln(C_0/C)$ of QB solution under sunlight irradiation over various catalysts; (c) UV-vis absorption spectrum of the QB solution in the presence of S2.

Fig. 14 (a) Time-course variation of (a) C/C_0 and (b) $\ln(C_0/C)$ of RhB solution under sunlight irradiation over various catalysts; (c) UV-vis absorption spectrum of the RhB solution in the presence of S2.

Fig. 15 Cycling runs in the photocatalytic degradation of RhB with Bi_2WO_6/BiOCl (S2) as the photocatalyst under visible light irradiation.

Fig. 16 First-principles results of the Bi_2WO_6-BiOCl heterojunction. (a) Crystal structures of the pristine Bi_2WO_6 and BiOCl, and the Bi_2WO_6-BiOCl heterojunction. The interface is shown as ball and stick model. Purple, green, red and blue atoms represent Bi, Cl, O, and W, respectively. (b)–(d) the band structures of the Bi_2WO_6, BiOCl, and the Bi_2WO_6-BiOCl heterojunction. Horizontal dashed lines represent Fermi levels.

Fig. 17 Time course of the photodegradation of QB over the as-prepared Bi_2WO_6/BiOCl (S2) in the presence of various radicals scavengers.

Fig. 18 Transient photocurrent responses of the BiOCl, Bi2WO_6 and BiOCl-Bi2WO_6 samples in 0.5 M Na_2SO_4 aqueous solutions under visible irradiation at 0.5 V vs. Ag/AgCl.